

PAPER

[View Article Online](#)
[View Journal](#) | [View Issue](#)Cite this: *Dalton Trans.*, 2025, **54**,
2985Ferroelectricity and piezoelectric energy harvesting
of an $A_3M_2X_9$ -type 0D bromobismuthate hybrid with
a bulky organic quaternary amine†Namonarayan Meena,^{‡a} Supriya Sahoo,^{id} ^{‡a} Nilotpal Deka,^{id} ^a Vinayak B. Gadagin,^a
Jan K. Zaręba^{id} *^b and Ramamoorthy Boomishankar^{id} *^a

Organic–inorganic hybrid ferroelectric compounds of the halobismuthate family have emerged as a focal point of research owing to their reduced toxicity and distinctive optical characteristics. This study presents a novel ammonium hybrid perovskite, $[BPMBDMA][Bi_2Br_9]$, which exhibits both ferro- and piezoelectric properties and crystallizes in the polar noncentrosymmetric $Pca2_1$ space group. The nonlinear optical (NLO) activity of $[BPMBDMA][Bi_2Br_9]$ was corroborated through second harmonic generation measurements evidencing its noncentrosymmetric structure, which was further substantiated by piezoresponse force microscopy analyses. Ferroelectric P – E hysteresis loop investigations conducted on a thin film sample of $[BPMBDMA][Bi_2Br_9]$ revealed a saturation polarization (P_s) as much as $11.30 \mu\text{C cm}^{-2}$ at ambient temperature. To explore the piezoelectric energy harvesting capabilities of $[BPMBDMA][Bi_2Br_9]$, composite materials were fabricated using polylactic acid (PLA) as a matrix. Notably, a device comprising 10 wt% $[BPMBDMA][Bi_2Br_9]$ in PLA demonstrated a remarkable output voltage of 24.6 V and a peak power density of $13.65 \mu\text{W cm}^{-2}$. The practical applicability of this device's output performance was further evaluated through a capacitor charging experiment, wherein a $10 \mu\text{F}$ capacitor was charged within 160 seconds.

Received 18th November 2024,
Accepted 30th December 2024

DOI: 10.1039/d4dt03225j

rsc.li/dalton

Introduction

Hybrid organic–inorganic perovskites (HOIPs) are an attractive class of compounds owing to their facile solution-phase synthesis and efficient functional behavior originating from their unique electronic and optical properties.^{1–3} For example, the optical properties of HOIPs can be controlled to exhibit high absorption coefficients, tunable bandgaps, and superior light-harvesting capabilities through subtle synthetic modifications.^{4–6} Several HOIPs containing Pb^{2+} , Sn^{2+} , Mg^{2+} , Mn^{2+} , Bi^{3+} , etc. have been discovered with excellent multifunctional properties.^{7–11}

Ferroelectricity is a property of crystalline polar materials that exhibit switchable spontaneous polarization under the application of an external electric field.^{12,13} Materials exhibit-

ing ferroelectricity are excellent candidates for mechanical energy harvesting applications because of their intrinsic piezoelectric properties.^{5,14,15} These materials are used in various technological applications such as ferroelectric random access memory (*FeRAM*), memristors, transistors, piezoelectric energy harvesters, wearable electronics, etc.^{16–20} Several classes of materials, ranging from oxide-based ceramics to organic small molecules, have been extensively studied for their ferroelectric properties.^{21–23} Though ceramics are well explored as commercial ferroelectrics, organic ferroelectrics are probed for their lower toxicity and easy device fabrication procedures. However, organic materials possess disadvantages such as low T_c , moisture instability, and poor polarization characteristics.^{24–26} In this context, HOIPs with ferro- and piezoelectric properties are promising alternatives as they can exhibit the advantages of both traditional ceramics and flexible organic/polymeric systems, bridging the gap between these two material types.^{13,27–29}

Bi-derived HOIPs exhibiting ferro- and piezoelectric properties are highly desirable due to their robust polarization behavior and lower environmental impact.^{30–35} Halobismuthates (alongside haloantimonates, which are not the subject of this paper but are highly structurally related), represented by the general formula $R_aM_bX_{3b+a}$ (where R is an organic cation, M = Sb(III) or Bi(III), and X = Cl, Br, or I), have emerged as a versatile

^aDepartment of Chemistry and Centre for Energy Science, Indian Institute of Science Education and Research (IISER), Pune, Dr Homi Bhabha Road, Pune – 411008, India. E-mail: boomii@iiserpune.ac.in

^bInstitute of Advanced Materials, Wrocław University of Science and Technology, Wrocław-50-370, Poland. E-mail: jan.zareba@pwr.edu.pl

†Electronic supplementary information (ESI) available. CCDC 2403399 and 2403400. For ESI and crystallographic data in CIF or other electronic format see DOI: <https://doi.org/10.1039/d4dt03225j>

‡These authors contributed equally to this work.

class of hybrid materials exhibiting remarkable ferroelectric properties and potential applications in optoelectronics and switchable dielectric devices. These compounds have gained immense interest due to their rich structural diversity, ranging from 0D to 3D architectures, though ferroelectric properties are specifically observed in certain stoichiometric arrangements, including RMX_4 ,³⁶ $\text{R}_3\text{M}_2\text{X}_9$, R_2MX_5 ,³⁷ and $\text{R}_5\text{M}_2\text{X}_{11}$.³⁸ Among these, the crystallization behavior of $\text{R}_3\text{M}_2\text{X}_9$ compounds is remarkably diverse, occurring either as infinite 1D double chains, 2D layers, discrete bi-octahedral (0D) units, or tetra-octahedral (0D) units.³⁹ Ferroelectric properties are primarily observed in materials with 2D layered structures or 0D discrete bi-octahedral units.⁴⁰ The 2D configuration, common in chloride and bromide variants, typically incorporates small alkylammonium cations or unsubstituted rings.^{41,42} 0D bi-octahedral anionic structures, in turn, show less restriction regarding organic cation size and symmetry^{43,44} and also constitute a preferred arrangement for iodide-based $\text{R}_3\text{M}_2\text{X}_9$ ferroelectrics.⁴⁵ This paper aims to demonstrate that the bi-octahedral anionic Bi_2Br_9 structure can be effectively generated using a bulky, organic arm-asymmetric aromatic amine for the crystallization of the bromobismuthate hybrid.

Herein, we report a ferroelectric $\text{A}_3\text{M}_2\text{X}_9$ -type HOIP of the formula $[(p\text{-BrPh})(p\text{-MeBn})\text{NMe}_2]_3\cdot[\text{Bi}_2\text{Br}_9]\cdot\text{MeOH}$, containing a bulkier ammonium cation, $[(p\text{-BrPh})(p\text{-MeBn})\text{NMe}_2]$ ($(p\text{-BrPh})(p\text{-MeBn})\text{NMe}_2 = N\text{-}4\text{-bromophenyl-}N\text{-}(4\text{-methylbenzyl})\text{-}N,N\text{-dimethylammonium}$; further abbreviated as BPMBDMA, thus the overall compound as $[\text{BPMBDMA}]\cdot[\text{Bi}_2\text{Br}_9]$). The halogenobismuthate complex $[\text{BPMBDMA}]\cdot[\text{Bi}_2\text{Br}_9]$ crystallizes in the polar orthorhombic $Pca2_1$ space group, and its non-centrosymmetric nature was confirmed through second harmonic generation (SHG) measurements. The $P\text{-}E$ hysteresis loop measurements of $[\text{BPMBDMA}]\cdot[\text{Bi}_2\text{Br}_9]$ resulted in a saturation polarization of $11.30\text{ }\mu\text{C cm}^{-2}$. The ferro- and piezoelectric properties of $[\text{BPMBDMA}]\cdot[\text{Bi}_2\text{Br}_9]$ were further corroborated by characteristic amplitude-bias butterfly and phase-bias hysteresis loops obtained from piezoresponse force microscopy studies. Piezoelectric energy harvesting experiments were conducted on polylactic acid (PLA) polymer composites containing this material, yielding a maximum output voltage of 24.6 V and a power density of $13.65\text{ }\mu\text{W cm}^{-2}$ for the best-performing 10 wt% device. Additionally, the electrical energy harvested from the 10 wt% $[\text{BPMBDMA}]\cdot[\text{Bi}_2\text{Br}_9]$ -PLA composite device was successfully used to charge a 10 μF capacitor.

Results and discussion

The 0D hybrid perovskite $[\text{BPMBDMA}]\cdot[\text{Bi}_2\text{Br}_9]$ was synthesized by adding Bi_2O_3 in HBr to an acetonitrile solution containing 4-methylbenzyl bromide and 4-bromo- N,N -dimethylaniline. Single-crystal X-ray diffraction (SCXRD) analysis of the $[\text{BPMBDMA}]\cdot[\text{Bi}_2\text{Br}_9]$ crystals revealed that the compound crystallizes in the polar noncentrosymmetric $Pca2_1$ space group at both 150 K and 298 K. The asymmetric unit of the $[\text{BPMBDMA}]\cdot[\text{Bi}_2\text{Br}_9]$ compound consists of three ammonium

cations supported by one $[\text{Bi}_2\text{Br}_9]^{3-}$ counterion (Fig. 1a, the disordered solvent methanol molecule has been omitted for clarity). The bismuth ions are located in a hexa-coordinated bi-octahedral environment, giving rise to an $\text{A}_3\text{M}_2\text{X}_9$ -type hybrid organic-inorganic system. Three Br-atoms bridge two Bi-centers, with Bi-Br-Bi angles ranging from 81.056° to 83.104° and Bi-Br bond lengths between 2.90 Å and 3.15 Å (Fig. 1b), which are significantly longer than the terminal Bi-Br bonds (2.67 Å–2.79 Å) (Fig. 1b). The trigonal symmetry of the anionic M_2X_9 moiety, combined with the bulky cations, gives the overall asymmetry to the compound, making it suitable for ferro- and piezoelectric investigations. The ionic and hydrogen bonding ($\text{C-H}\cdots\text{Br}$) interactions in $[\text{BPMBDMA}]\cdot[\text{Bi}_2\text{Br}_9]$ are responsible for its robust long-range polar order. A closer look at the H-bonding interactions present in $[\text{BPMBDMA}]\cdot[\text{Bi}_2\text{Br}_9]$ revealed that each $[\text{Bi}_2\text{Br}_9]^{3-}$ unit is connected to five ammonium units through H-bonding interactions. The $-\text{CH}_3$ and $-\text{CH}_2-$ protons of three ammonium counteranions interact with the Br atoms of the bi-octahedral $[\text{Bi}_2\text{Br}_9]^{3-}$ anions, forming 1D chains that grow along the c -axis. Additionally, another ammonium cation acts as a bridge between two adjacent H-bonded 1D chains. The phenyl and $-\text{CH}_3$ hydrogen atoms of this bridging ammonium cation are H-bonded to both terminal and bridging $[\text{Bi}_2\text{Br}_9]^{3-}$ anions, with $\text{C-H}\cdots\text{Br}$ bond lengths ranging from 2.73 Å to 2.85 Å. Together, these interactions form a 2D H-bonded network extending along the bc -plane (Fig. 1c). To gain further insight into the different types of interactions present in $[\text{BPMBDMA}]\cdot[\text{Bi}_2\text{Br}_9]$, Hirshfeld surface (HS) analysis was performed (Fig. 1d). The associated 2D fingerprint plots were also generated, revealing the percentages of various interactions within the molecule. In $[\text{BPMBDMA}]\cdot[\text{Bi}_2\text{Br}_9]$, $\text{C-H}\cdots\text{Br}$ interactions are predominant, contributing to 53.7% of the overall surface contacts. The

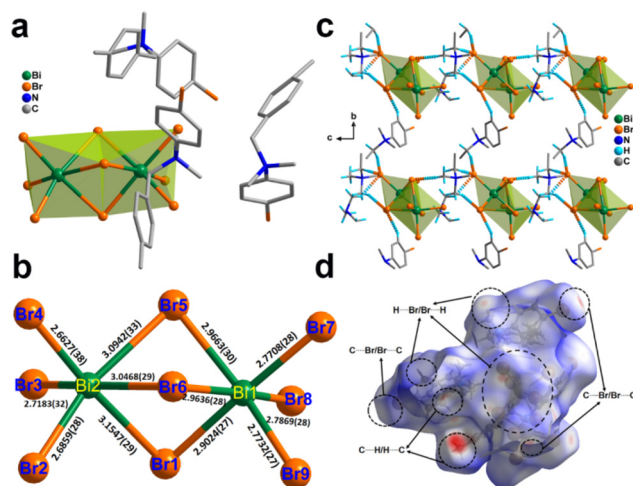


Fig. 1 (a) Asymmetric unit of $[\text{BPMBDMA}]\cdot[\text{Bi}_2\text{Br}_9]$. (b) Bi-octahedral Bi_2Br_9 unit with Bi and Br bond distances. (c) $\text{C-H}\cdots\text{Br}$ H-bonding interactions present in $[\text{BPMBDMA}]\cdot[\text{Bi}_2\text{Br}_9]$. The phenyl rings are omitted for clarity. (d) d_{norm} -mapped HS showing different interactions present in $[\text{BPMBDMA}]\cdot[\text{Bi}_2\text{Br}_9]$.

Hirshfeld surface interaction study also revealed that the O atom of crystallized solvent methanol has very little interaction (Fig. S3, S4 and Tables S3, S4†).

The bulk purity of [BPMBDMA]·[Bi₂Br₉] was confirmed through powder X-ray diffraction (PXRD) analysis, which showed a good match with the simulated pattern. The elemental analysis studies also match well with the calculated percentage of elements in [BPMBDMA]·[Bi₂Br₉]. Thermogravimetric analysis (TGA) and differential thermal analysis (DTA) indicated that [BPMBDMA]·[Bi₂Br₉] is stable up to approximately 410 K (Fig. S6†). To investigate potential temperature-dependent structural changes, differential scanning calorimetry (DSC) measurements were performed, revealing no heat anomalies up to the material's melting point. Additionally, solid-state UV-visible spectroscopy was conducted to explore the optical properties of [BPMBDMA]·[Bi₂Br₉], showing a pronounced absorption peak starting at 370 nm. The bandgap, derived from a Tauc plot, was calculated to be 2.7 eV, comparable to the bandgaps observed in many organic–inorganic lead-based ferroelectric semiconductors.⁴⁶ Furthermore, the asymmetry in [BPMBDMA]·[Bi₂Br₉] is validated by second harmonic generation (SHG) measurements at room temperature. Unsieved powder samples of [BPMBDMA]·[Bi₂Br₉] exhibited an SHG efficiency of 0.11 relative to the reference potassium dihydrogen phosphate (KDP) (Fig. 2a).

To confirm the dielectric properties of [BPMBDMA]·[Bi₂Br₉], temperature-dependent dielectric permittivity measurements were carried out from 298 K to 365 K across a frequency range of 10 Hz–10⁵ Hz on compacted pellet samples. The real part of the dielectric permittivity (ϵ') was found to be 7.49 at room temperature and at a frequency of 100 kHz. An increasing trend in the dielectric constant was observed as the temperature approached the melting point, attributed to thermally activated free carriers due to ion mobility within the material (Fig. S8a†). Similar trends were observed as well in the frequency-dependent dielectric profiles (Fig. S8b†). The ϵ' values increased as the frequency decreased from 10⁵ to 10¹ Hz, indicating the involvement of all types of polarization mechanisms (electronic, ionic, orientational, and space charge polarization) at lower frequencies. The temperature- and frequency-dependent dielectric loss profiles followed

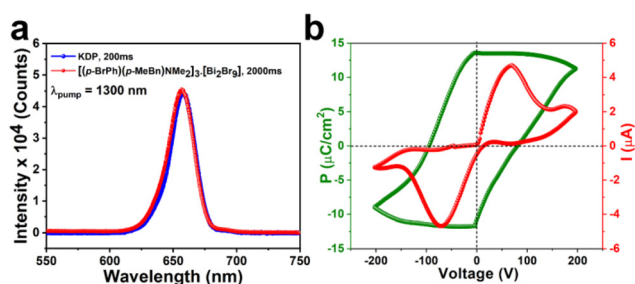


Fig. 2 (a) Comparison of the SHG emission profiles of [BPMBDMA]·[Bi₂Br₉] and the reference KDP sample. (b) *P*–*E* hysteresis loop for [BPMBDMA]·[Bi₂Br₉] at room temperature.

trends similar to those observed for dielectric permittivity (Fig. S9†).

Ferroelectric *P*–*E* hysteresis loop measurements performed on the thin film sample of [BPMBDMA]·[Bi₂Br₉] on an indium tin oxide (ITO)-coated surface revealed a saturation polarization of 11.30 μC cm^{−2}, confirming the bulk polar nature of the material (Fig. 2b). The bulk polarization of [BPMBDMA]·[Bi₂Br₉] was further validated with the rectangular *P*–*E* hysteresis loops obtained at different frequencies and applied voltages (Fig. S11†). Additionally, the ferroelectric fatigue measurements revealed no notable change in the saturation polarization values up to 10⁶ measurement cycles, highlighting the intact polarization properties of [BPMBDMA]·[Bi₂Br₉] (Fig. S12†). Consistent with the bulk polarization results, the microscopic polarization properties of [BPMBDMA]·[Bi₂Br₉] were further validated through piezoresponse force microscopy (PFM) studies. The PFM-derived amplitude and phase images of ±90 V showed the presence of differently oriented domains within the material (Fig. 3a and b). Additionally, amplitude-bias butterfly loops and phase-bias hysteresis loops recorded at a single point on the thin film surface using an applied DC bias of ±40 and ±50 V further corroborated its piezoelectric and ferroelectric properties (Fig. 3c, d and S13†). The converse piezoelectric coefficient (d_{33}) was calculated to be in the range of 16.5–18.5 pm V^{−1} based on the slope of the amplitude-bias butterfly loop.

Driven by the ferro- and piezoelectric properties of [BPMBDMA]·[Bi₂Br₉], polymer composite films were fabricated using the piezoelectric polymer polylactic acid (PLA). Various weight percentages (5, 10, 15, and 20 wt%) of [BPMBDMA]·[Bi₂Br₉] were dispersed in a chloroform solution of PLA. The resulting homogeneous solutions were poured into Petri dishes and dried to form flexible composite films (Fig. S15†). After drying, the [BPMBDMA]·[Bi₂Br₉]–PLA compo-

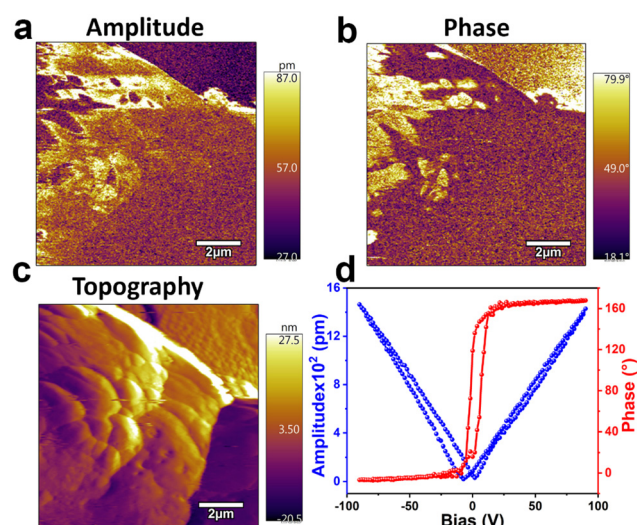


Fig. 3 PFM-derived (a) amplitude image and (b) phase image. (c) Topography of [BPMBDMA]·[Bi₂Br₉]. (d) Amplitude-bias "butterfly" (blue) and phase-bias "hysteresis" (red) loops of [BPMBDMA]·[Bi₂Br₉].

site films were peeled off and characterized (Fig. S16†). From the PXRD analyses, it has been confirmed that the ferroelectric molecule retained its original crystalline structure in all the composite films. Additionally, an increase in peak intensity was observed with higher crystallite loadings (from 5 to 20 wt%) (Fig. S17†). Field emission scanning electron microscopy (FE-SEM) revealed uniform dispersion of ferroelectric crystallites in the films of up to 10 wt%, while agglomeration occurred at a higher loading of 20 wt% [BPMBDMA]·[Bi₂Br₉]-PLA composite.

Furthermore, to optimize the frequency and force of measurement, the frequency- and force-dependent voltage outputs were collected. The 10 wt% [BPMBDMA]·[Bi₂Br₉]-PLA device was observed to give the maximum output voltage with 21 N of force at 10 Hz frequency (Fig. S18 and S19†). Therefore, all the remaining piezoelectric nanogenerator measurements were performed with an optimized applied external load of 21 N at a constant frequency of 10 Hz for the [BPMBDMA]·[Bi₂Br₉]-PLA composite devices. For the batch of the [BPMBDMA]·[Bi₂Br₉]-PLA composite devices, the maximum open-circuit peak-to-peak voltage (V_{pp}) was found to be 24.6 V for the 10 wt% device. In comparison, the 5, 15, and 20 wt% [BPMBDMA]·[Bi₂Br₉]-PLA devices exhibited V_{pp} values of 13.76 V, 18.34 V, and 7.17 V, respectively (Fig. 4a and S15†). The reduction in open-circuit voltages for the 15 and 20 wt% devices is likely due to dipole cancellation caused by the overcrowding of [BPMBDMA]·[Bi₂Br₉] crystallites within the PLA matrix.⁴⁷ In contrast, a minimal output voltage of 2 V was observed for the neat PLA device, attributed to its inherent

piezoelectric properties. This confirms that the enhanced voltage outputs in the composite devices are due to the ferroelectric and piezoelectric nature of the embedded organic-inorganic hybrid material in the PLA matrix. The short-circuit peak-to-peak currents (I_{pp}) for all the [BPMBDMA]·[Bi₂Br₉]-PLA composite devices were also calculated by connecting an external load resistance of 1 M Ω using Ohm's law. The calculated currents were found to be 6.76, 12.01, 9.49, and 2.67 μ A for the 5, 10, 15, and 20 wt% devices, respectively (Fig. 4b and S16†).

To assess their practical utility, voltage drops across all the [BPMBDMA]·[Bi₂Br₉]-PLA composite devices were measured over a range of load resistances from 0.11 M Ω to 88 M Ω (Fig. 4c). The voltage drop increased with rising resistance up to 22 M Ω and then saturated at higher resistances. The corresponding current profile followed an inverse trend relative to the voltage-drop profile (Fig. S18†). From this peak-voltage drop, the maximum peak power density for the best-performing 10 wt% [BPMBDMA]·[Bi₂Br₉]-PLA device was calculated to be 13.65 μ W cm⁻² at a threshold load resistance of 1 M Ω (Fig. 4c). Additionally, cyclic piezoelectric measurements on the best-performing 10 wt% composite device showed no notable changes in the open-circuit voltage output over up to 4000 cycles (Fig. S24†).

Furthermore, the capacitor charging capability of the 10 wt% [BPMBDMA]·[Bi₂Br₉]-PLA device was evaluated by connecting it to a four-diode bridge rectifier circuit, which converts AC voltages into DC outputs. It was observed that the 10 wt% [BPMBDMA]·[Bi₂Br₉]-PLA device successfully accumulated a charge of 2.03 μ C in a 10 μ F capacitor within 160 seconds (Fig. 4d). The corresponding voltage and calculated energy were of the order of 0.2 V and 0.2 μ J, respectively (Fig. S25† and 4d).

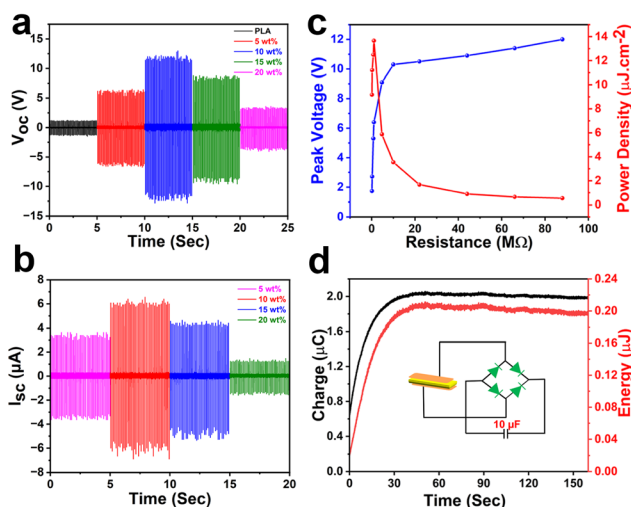


Fig. 4 (a) Open-circuit peak-to-peak voltages obtained for the [BPMBDMA]·[Bi₂Br₉]-PLA composite devices. (b) Short-circuit current profiles for the [BPMBDMA]·[Bi₂Br₉]-PLA composite devices. (c) Resistance-dependent voltage drop for the 10 wt% [BPMBDMA]·[Bi₂Br₉]-PLA composite device and the calculated power density across the load resistances. (d) Charge and energy stored in a 10 μ F capacitor by using the champion 10 wt% [BPMBDMA]·[Bi₂Br₉]-PLA composite device. The inset shows a schematic of the four-diode bridge rectifier circuit utilized for capacitor charging experiments.

Conclusions

In summary, a new hybrid ammonium halogenobismuthate [BPMBDMA]·[Bi₂Br₉], crystallizing in the polar point group *Pca*2₁, has been successfully synthesized. The second harmonic generation (SHG) activity of [BPMBDMA]·[Bi₂Br₉] was found to be 0.11 relative to the KDP reference sample. The ferroelectric nature of [BPMBDMA]·[Bi₂Br₉] is probed through *P-E* hysteresis loop analysis on its drop-cast thin film, which exhibited a saturation polarization of 11.30 μ C cm⁻² at room temperature. The PFM spectroscopic measurements on the crystalline thin film sample displayed characteristic butterfly and hysteresis loops, further supporting its ferro- and piezoelectric properties. Moreover, the implementation of [BPMBDMA]·[Bi₂Br₉] for mechanical energy harvesting applications in the form of PLA polymer composites resulted in a maximum peak-to-peak voltage of 24.6 V. The maximum power density was calculated to be 13.65 μ W cm⁻² for the optimal 10 wt% [BPMBDMA]·[Bi₂Br₉]-PLA device. The capacitor charging capabilities of this device were also demonstrated. These findings provide a promising platform for designing new lead-free ammonium-based perovskites using bismuth as

a metal centre, which is significantly less toxic than lead-based materials, paving the way for future self-powered electronic devices.

Author contributions

R. B., N. M., and S. S. designed the project. R. B. directed the project. N. M. prepared the samples. N. M., S. S., N. D., V. B. G. and J. K. Z. performed the measurements. N. M., S. S., N. D., and R. B. wrote the original manuscript. V. B. G. and J. K. Z. reviewed and edited the manuscript. All the authors discussed the results and contributed sincerely to the preparation of the manuscript.

Data availability

The data supporting this article have been included as part of the ESI† Crystallographic data have been deposited at the CCDC under 2403399 (150 K data) and 2403400 (298 K data).

Conflicts of interest

There are no conflicts to declare.

Acknowledgements

R. B. thanks SERB, India, via Grant No. CRG/2023/000582 and SERB, India, for the Science and Technology Award for Research (STAR) via Grant No. STR/2021/000016. N. D. thanks PMRF, India, for the fellowship. J. K. Z. acknowledges financial support from the Wroclaw University of Science and Technology and Academia Iuvenum.

References

- 1 K. Liu, Y. Jiang, Y. Jiang, Y. Guo, Y. Liu and E. Nakamura, *J. Am. Chem. Soc.*, 2018, **141**, 1406–1414.
- 2 M. Faustini, L. Nicole, E. Ruiz-Hitzky and C. Sanchez, *Adv. Funct. Mater.*, 2018, **28**, 1704158.
- 3 J.-B. Li, Z.-K. Jiang, R. Wang, J.-Z. Zhao and R. Wang, *npj Comput. Mater.*, 2023, **9**, 62.
- 4 H. D. Pham, L. Xianqiang, W. Li, S. Manzhos, A. K. K. Kyaw and P. Sonar, *Energy Environ. Sci.*, 2019, **12**, 1177–1209.
- 5 T. Vijayakanth, D. J. Liptrot, E. Gazit, R. Boomishankar and C. R. Bowen, *Adv. Funct. Mater.*, 2022, **32**, 2109492.
- 6 W.-P. Zhao, C. Shi, A. Stroppa, D. Di Sante, F. Cimpoesu and W. Zhang, *Inorg. Chem.*, 2016, **55**, 10337–10342.
- 7 R. A. DeCrescent, N. R. Venkatesan, C. J. Dahlman, R. M. Kennard, X. Zhang, W. Li, X. Du, M. L. Chabiny, R. Zia and J. A. Schuller, *Sci. Adv.*, 2020, **6**, eaay4900.
- 8 L. Caussin, A. Jouaiti, D. Chartrand, W. Skene and S. Ferlay, *Dalton Trans.*, 2024, **53**, 12755–12763.
- 9 Y. Asensio, H. Bahmani Jalali, S. Marras, M. Gobbi, F. Casanova, A. Mateo-Alonso, F. Di Stasio, I. Rivilla, L. E. Hueso and B. Martín-García, *Adv. Opt. Mater.*, 2024, **12**, 2400554.
- 10 N. Meena, S. Sahoo, N. Deka, J. K. Zaręba and R. Boomishankar, *Inorg. Chem.*, 2024, **63**, 9245–9251.
- 11 C.-R. Huang, X. Luo, X.-G. Chen, X.-J. Song, Z.-X. Zhang and R.-G. Xiong, *Natl. Sci. Rev.*, 2021, **8**, nwaa232.
- 12 Q. Pan, Z.-X. Gu, R.-J. Zhou, Z.-J. Feng, Y.-A. Xiong, T.-T. Sha, Y.-M. You and R.-G. Xiong, *Chem. Soc. Rev.*, 2024, **53**, 5781–5861.
- 13 W. Zhang and R.-G. Xiong, *Chem. Rev.*, 2012, **112**, 1163–1195.
- 14 S. Sahoo, T. Vijayakanth, P. Kothavade, P. Dixit, J. K. Zaręba, K. Shanmuganathan and R. Boomishankar, *ACS Mater. Au*, 2021, **2**, 124–131.
- 15 R. Gupta, S. Sahoo, S. Deswal, P. Kothavade, P. Dixit, J. K. Zaręba, K. Shanmuganathan and R. Boomishankar, *Chem. – Asian J.*, 2021, **16**, 4122–4129.
- 16 S. Sahoo, P. A. Kothavade, D. R. Naphade, A. Torris, B. Praveenkumar, J. K. Zaręba, T. D. Anthopoulos, K. Shanmuganathan and R. Boomishankar, *Mater. Horiz.*, 2023, **10**, 3153–3161.
- 17 S. Sahoo, N. Deka, R. Panday and R. Boomishankar, *Chem. Commun.*, 2024, **60**, 11655–11672.
- 18 M. E. Lines and A. M. Glass, *Principles and applications of ferroelectrics and related materials*, Oxford university press, 2001.
- 19 J. Scott, *Science*, 2007, **315**, 954–959.
- 20 H. Ishiura, *J. Nanosci. Nanotechnol.*, 2012, **12**, 7619–7627.
- 21 Z.-H. Lin, Y. Yang, J. M. Wu, Y. Liu, F. Zhang and Z. L. Wang, *J. Phys. Chem. Lett.*, 2012, **3**, 3599–3604.
- 22 H. Jaffe, *J. Am. Ceram. Soc.*, 1958, **41**, 494–498.
- 23 S. Sahoo, S. Mukherjee, V. B. Sharma, W. I. Hernández, A. C. Garcia-Castro, J. K. Zaręba, D. Kabra, G. Vaitheeswaran and R. Boomishankar, *Angew. Chem., Int. Ed.*, 2024, **63**, e202400366.
- 24 S. Horiuchi and Y. Tokura, *Nat. Mater.*, 2008, **7**, 357–366.
- 25 K. Asadi, M. Li, P. W. Blom, M. Kemerink and D. M. De Leeuw, *Mater. Today*, 2011, **14**, 592–599.
- 26 N. Deka, S. Sahoo, A. S. Goswami, J. K. Zaręba and R. Boomishankar, *Cryst. Growth Des.*, 2024, **24**, 6763–6770.
- 27 P. Jain, N. S. Dalal, B. H. Toby, H. W. Kroto and A. K. Cheetham, *J. Am. Chem. Soc.*, 2008, **130**, 10450–10451.
- 28 P. Jain, V. Ramachandran, R. J. Clark, H. D. Zhou, B. H. Toby, N. S. Dalal, H. W. Kroto and A. K. Cheetham, *J. Am. Chem. Soc.*, 2009, **131**, 13625–13627.
- 29 S. Ghosh, D. Di Sante and A. Stroppa, *J. Phys. Chem. Lett.*, 2015, **6**, 4553–4559.
- 30 K. Mencil, V. Kinzhybalov, R. Jakubas, J. K. Zaręba, P. Szklarz, P. Durlak, M. Drozd and A. Piecha-Bisiorek, *Chem. Mater.*, 2021, **33**, 8591–8601.
- 31 M. Lyu, J. H. Yun, P. Chen, M. Hao and L. Wang, *Adv. Energy Mater.*, 2017, **7**, 1602512.
- 32 Q. Fan, G. V. Biesold-McGee, J. Ma, Q. Xu, S. Pan, J. Peng and Z. Lin, *Angew. Chem., Int. Ed.*, 2020, **59**, 1030–1046.

- 33 R. Jakubas, A. Gągor, M. J. Winiarski, M. Ptak, A. Piecha-Bisiorek and A. Cizman, *Inorg. Chem.*, 2019, **59**, 3417–3427.
- 34 A. Piecha-Bisiorek, A. Gągor, R. Jakubas, A. Cizman, R. Janicki and W. Medycki, *Inorg. Chem. Front.*, 2017, **4**, 1281–1286.
- 35 S. Sahoo, N. Deka and R. Boomishankar, *CrystEngComm*, 2022, **24**, 6172–6177.
- 36 R. Jakubas, Z. Ciunik and G. Bator, *Phys. Rev. B:Condens. Matter Mater. Phys.*, 2003, **67**, 024103.
- 37 W. Bi, N. Leblanc, N. Mercier, P. Auban-Senzier and C. Pasquier, *Chem. Mater.*, 2009, **21**, 4099–4101.
- 38 A. Piecha, A. Białońska and R. Jakubas, *J. Phys.: Condens. Matter*, 2008, **20**, 325224.
- 39 R. Jakubas, M. Rok, K. Mencil, G. Bator and A. Piecha-Bisiorek, *Inorg. Chem. Front.*, 2020, **7**, 2107–2128.
- 40 R. Jakubas, J. Lefebvre, H. Fontaine and P. Francois, *Solid State Commun.*, 1992, **81**, 139–143.
- 41 J. Zaleski, C. Pawlaczyk, R. Jakubas and H. Unruh, *J. Phys.: Condens. Matter*, 2000, **12**, 7509.
- 42 M. Wojciechowska, A. Gągor, A. Piecha-Bisiorek, R. Jakubas, A. Cizman, J. K. Zareba, M. Nyk, P. Zieliński, W. Medycki and A. Bil, *Chem. Mater.*, 2018, **30**, 4597–4608.
- 43 Z. Sun, A. Zeb, S. Liu, C. Ji, T. Khan, L. Li, M. Hong and J. Luo, *Angew. Chem.*, 2016, **128**, 12033–12037.
- 44 C. Ji, Z. Sun, A. Zeb, S. Liu, J. Zhang, M. Hong and J. Luo, *J. Phys. Chem. Lett.*, 2017, **8**, 2012–2018.
- 45 P. Szklarz, A. Gągor, R. Jakubas, P. Zieliński, A. Piecha-Bisiorek, J. Cichos, M. Karbowiak, G. Bator and A. Cizman, *J. Mater. Chem. C*, 2019, **7**, 3003–3014.
- 46 S. Liu, F. Zheng, I. Grinberg and A. M. Rappe, *J. Phys. Chem. Lett.*, 2016, **7**, 1460–1465.
- 47 M. Arous, H. Hammami, M. Lagache and A. Kallel, *J. Non-Cryst. Solids*, 2007, **353**, 4428–4431.